

Performance and Durability Tests of Smart Icephobic Coatings to Reduce Ice Adhesion

Zaid A. Janjua¹, Barbara Turnbull¹, Kwang-Leong Choy², Christos Pandis², Junpeng Liu¹, Xianghui Hou¹, and Kwing-So Choi¹.

¹ Faculty of Engineering, University of Nottingham.

² Institute for Materials Discovery, University College London (UCL).

Keywords: Icephobic coatings, Runback icing, Aerofoil icing, Centrifuge.

The accretion of ice can damage applications ranging from power lines and shipping decks; to wind turbines and rail infrastructure. In particular on aircraft, it can change aerodynamic characteristics, greatly affecting the flight safety. Commercial aircraft are therefore required to be equipped with de-icing devices, such as heating mats over the wings. The application of icephobic coatings near the leading edge of a wing can in theory reduce the high power requirements of heating mats, which melt ice that forms there. Such coatings are effective in preventing the accretion of runback ice, formed from airborne supercooled droplets, or the water that the heating mats generate as it is sheared back over the wing's upper surface. However, the durability and the practicality of applying them over a large wing surface have been prohibitive factors in deploying this technology so far.

Here, we evaluated the ice adhesion strength of four non-conductive coatings and seven thermally conductive coatings by shearing ice samples from coated plates by spinning them in a centrifuge device. The durability of the coating performance was also assessed by repeating the tests, each time regrowing ice samples on the previously-used coatings. Contact angle parameters of each coating were tested for each test to determine influence on ice adhesion strength. The results indicate that contact angle hysteresis is a crucial parameter in determining icephobicity of a coating and *hydrophobicity* is not necessarily linked to *icephobicity*.

1. Introduction

Ice formation on an aircraft in flight reduces the aerodynamic control, fuel efficiency and lift characteristics of the system¹. The development of a smart anti-ice coating, that is both icephobic to reduce adhesion strength and can be heated to reduce the amount of ice that can accrete in the first place, is considered as a crucial step in reducing the high power usage of currently operational electro-thermal mats. These mats operate only over a small portion of the wing surface near the leading edge and, by melting ice there they can generate water which may then refreeze on the extensive unheated wing surface. Thus, coatings present an opportunity to reduce icing over all parts of the wing.

Kasaai and Farzaneh (2004)² extensively review various methods for evaluating ice adhesion strength. Approaches include a parallel plate type shear rig experimental technique developed by the NASA Lewis Icing Research Tunnel³, a plunger and pressure tube arrangement⁴, destructive wedge testing using weights⁵, a modified Zero-Degree cone test⁶ and an electro-magnetic shaker system⁷. Most of these devices are however complex and exhibit high variability in their measurements. The approach described here draws upon the design and strategy previously

implemented by Laforte & Beisswenger (2005)⁸ and Kulinich & Farzaneh (2009)⁹, employing a spinning centrifuge to determine the rotation rate at which the centrifugal acceleration overcame the ice adhesion strength. This technique is simple and significantly leads to a relatively low variability in measurements (~18%)⁸, and further permits atmospheric icing temperature conditions to be replicated by deploying the system within an environment-controlled chamber.

Ice accretion is problematic also in other engineering applications such as power cables, radio masts or wind turbines¹⁰. Research into finding icephobic coatings has been active since the 1960s¹¹, but several issues persist: in particular, the durability of coatings and the practicalities of applying to extensive areas on structural surfaces exposed to rugged environments. Several materials have been proposed as icephobic coatings including polytetrafluoroethylene (PTFE)^{12,13}, fluorinated polymethylsiloxane and octavinyl-polyhedral oligomeric silsesquioxanes (OVPOSS)¹⁴⁻¹⁶, Al₂O₃ nanoparticle in silicone rubber solution¹⁷, combination of hydrogen peroxide and an acid (nitric or hydrochloric)¹⁸, silica nanoparticles and polymethyl methacrylate (PMMA)¹⁹ and sol-gel coatings containing tetraethylorthosilicate (TEOS) and 3-glycidylpropyl trimethoxy silane (GPTMS)⁴.

By investigating this range of coatings, we aim to add further evidence to the debate over the correlation between icephobicity and hydrophobicity²⁰⁻²². In particular, we look at the contact angle hysteresis for a surface¹²⁻¹⁵ to evaluate its link to icephobicity.

The aim of this work was thus to evaluate the performance of two types of coating, one set using silica-based nano-particles the other set employing carbon nano-tubes, with the potential to become icephobic smart coatings to reduce runback ice accretion on aircraft wings. Each coating was characterised for contact angle (CA) (advancing, receding and CA hysteresis), surface

roughness and the adhesion strength of an ice sample grown in controlled conditions. These tests were repeated, reusing each coating sample by growing new ice on it after detachment of the previous ice sample, to evaluate the deterioration in performance of the coating with use.

2. Coating Design

In the present work we investigate two approaches to coating design. First, the approach of Zhang et al. (2015)²³ who prepared superhydrophobic coatings using silica nanoparticles immersed in chloroform and spin coated onto glass slides has been adopted and developed. Results showed reduced wetting of water droplets on coated surfaces.

In an alternative approach to designing the coating, it was noted that the presence of reinforced materials such as nanoparticles, nanowires and nanotubes in a matrix (typically polymer) increases the surface roughness of the nanocomposites, thus resulting in higher contact angles with water droplets. For example, silica reinforced acrylic polymer composites can exhibit superhydrophobic surfaces and anti-icing capability upon the impact of supercooled water²⁴. The surface morphology of the coating also strongly influences the anti-icing capability. Nanocomposites with different surface roughness have been prepared by varying the amount of ZrO₂/fluoropolymer nanopowder suspension and mixing with perfluoroalkyl methacrylic copolymer have also been fabricated using spraying or spin-coating, followed by heat treatment to remove residual solvents²⁵. A second batch of coatings prepared by the authors uses surface texturing and chemical modification of the aluminium substrate before deposition of carbon nanotube composite coatings to prevent ice adhesion.

Eleven coatings have been developed with potential anti-icing capability and tested in this work. These coatings were applied to an Aluminium 6082, with T651 temper, polished substrate plate

with thickness 1 mm and total surface area 1000 mm², on which ice could be grown and the sample plate fixed to the rotor of the centrifuge to measure adhesion strength. Of a total of 31 substrate plates, 20 were left uncoated for sensitivity tests. The remaining 11 plates were coated with the eleven coatings to be tested which are divided into two groups: Group 1 – A, B, C and D and Group 2 – E, F, G, H, I, J and K.

Group 1: All the four samples (A, B, C and D) were fabricated using silica nanoparticles and polystyrene by a spin coating method. Silica nanoparticles and polystyrene were mixed together at weight ratio of 23.8:1 and dissolved into chloroform followed by stirring for about 1 hour at room temperature. The four thin film samples of A, B, C and D were deposited using silica nanoparticles/polystyrene solution by spin coating at 1500 rad/min for 1 minute onto Al alloy substrates. A heat treatment at 550 °C for 2 hours for sample C and D were performed. Then a surface modification with 1H,1H,2H,2H-perfluorooctyltriethoxysilane (PFTS) was performed using chemical vapour deposition method for all four samples.

Group 2: Samples E, F, G, H, I, J and K were prepared using carbon nanotube technology. The bare substrates were mechanically polished using a grinding machine with 1200 sand paper and subject to ultrasonic cleaning with acetone, ethanol and water for 10 minutes. The deposition method used was an eco-friendly, non-vacuum and cost-effective aerosol assisted deposition coating rig specifically set up for manufacturing of nanostructured carbon-based coatings for anti-icing applications (see Figure 1). The starting solution was prepared using an appropriate solvent as disperser of carbon nanotubes. The surfaces of multiwalled CNT (circa. diameter 9 nm, length 0.5-3µm) were functionalized with fluorosilane leading to the hydrophobic behavior. Prior to deposition, the final dispersion was placed in an ultrasonication bath for a few minutes to ensure good dispersion of carbon nanotubes. The content of carbon nanotubes was varied in order to study

their effect on surface roughness, anti-icing properties and electrical conductivity. Furthermore, in order to promote the adhesion between the coating and the aluminum substrate an interlayer with a thickness of 15-25 μ m of organic-based compound containing acetate was used prior to anti-icing coating deposition. Finally, from the selected samples, a final hydrophobic polymeric surface promoter layer was applied.

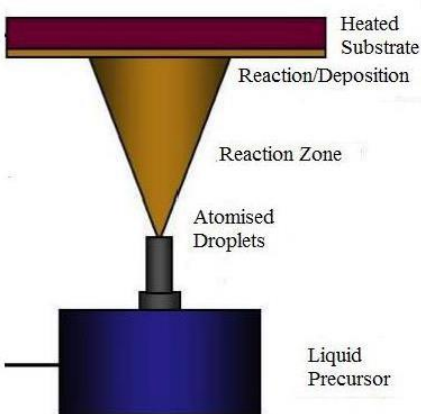


Figure 1. A schematic diagram of the Aerosol Assisted Deposition process.

Table 1 provides coating labels (used throughout the text) and their respective chemical composition, contact angle and surface roughness properties. All values are the average of three measurements.

Table 1. Coating label and its respective composition, contact angle and surface roughness properties. Uncoated characteristics are also shown.

Coating	Static Contact Angle °	Advancing Contact Angle °	Receding Contact Angle °	Contact Angle Hysteresis °	Surface Roughness (μ m)
---------	------------------------	---------------------------	--------------------------	----------------------------	------------------------------

Uncoated	Aluminium 6082-T651 tempered				
	95.8 ± 3.14	102.2 ± 4.53	33.1 ± 3.32	69.1 ± 5.62	0.295 ± 0.072
A	Silica nanoparticles and polystyrene (no heat treatment) with PFTS treatment				
	101.98 ± 1.96	110.67 ± 1.03	82.94 ± 4.86	27.73 ± 3.84	1.13 ± 0.13
B	Silica nanoparticles and polystyrene (no heat treatment) with PFTS treatment				
	100.36 ± 3.15	108.84 ± 0.72	82.65 ± 5.57	26.18 ± 5.03	1.07 ± 0.13
C	Silica nanoparticles and polystyrene (2 hours heat treatment at 550°C) with PFTS treatment				
	130.48 ± 3.84	132.66 ± 5.66	87.87 ± 4.75	44.79 ± 3.71	2.01 ± 0.12
D	Silica nanoparticles and polystyrene (2 hours heat treatment at 550°C) with PFTS treatment				
	135.12 ± 1.71	137.22 ± 3.41	92.43 ± 5.35	44.17 ± 2.16	2.06 ± 0.33
E	20% functionalised carbon nanotube content with use of an interlayer; no deposition of final surface promoter layer.				
	140.67 ± 2.65	143.56 ± 5.40	62.28 ± 4.15	81.27 ± 2.17	1.59 ± 0.19
F	20% functionalised carbon nanotube content with use of an interlayer; and with deposition of final surface promoter layer.				
	154.14 ± 1.63	157.81 ± 2.86	145.06 ± 4.38	12.75 ± 7.19	2.65 ± 0.41
G	10% functionalised carbon nanotube content with use of an interlayer; no deposition of final surface promoter layer.				
	112.97 ± 3.15	133.94 ± 2.63	57.55 ± 2.90	76.39 ± 4.58	1.43 ± 0.06
H	5% functionalised carbon nanotube content with use of an interlayer; no deposition of final surface promoter layer.				
	108.2 ± 0.85	129.82 ± 2.94	49.32 ± 1.55	80.5 ± 3.32	1.64 ± 0.26
I	2.5% functionalised carbon nanotube content with use of an interlayer; no deposition of final surface promoter layer.				
	110.86 ± 0.61	132.66 ± 1.43	34.18 ± 2.34	98.48 ± 2.74	1.60 ± 0.21
J	10% functionalised carbon nanotube content with use of an interlayer; and with deposition of final surface promoter layer.				
	108.13 ± 0.68	118.69 ± 0.42	34.11 ± 2.66	84.57 ± 2.69	1.43 ± 0.10

K	5% functionalised carbon nanotube content with use of an interlayer; and with deposition of final surface promoter layer.				
	159.7 ± 3.04	164.69 ± 3.05	138.60 ± 1.24	26.08 ± 3.29	3.22 ± 0.24

3. Experimental setup and procedure

To characterize the hydrophobicity and surface properties of the coatings static contact angle was measured using sessile drop technique²⁶ on NAVITAR 1x adapter 1-6015 goniometer. Images were processed using FTÅ200 software. Drop volume was kept constant at 10 μ L. Figure 2 shows static contact angle measurements of Coating E, F and G prior to any ice growth or detachment. From previous studies^{20–22}, we do not expect a clear link between hydrophobicity and icephobicity. Advancing angle was measured as the average of three consecutive values when drop volume was increased at 2 μ L/s. Receding contact angle was measured as the average of three consecutive values when drop volume was decreased and base diameter decreased at 2 μ L/sec. Room temperature was recorded at $25 \pm 0.3^\circ\text{C}$ with humidity 26%. Surface roughness of the 20 uncoated substrates was measured using a Mitutoyo SurfTest SV-622 profilometer. Figure 3 shows optical microscope images (at 20x magnification) of coatings E and G using Alicona InfiniteFocus Optical Microscope, with focus area 2 x 2 mm and characteristic wavelength $L_C = 250 \mu\text{m}$.

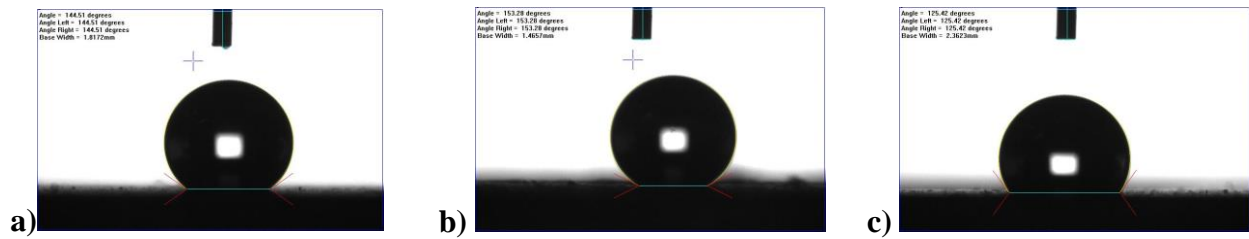


Figure 2. Static contact angle measurements for a) coating E - 20% functionalised carbon nanotube content with use of an interlayer; no deposition of final surface promoter layer, b) coating F - 20% functionalised carbon nanotube content with use of an interlayer; and with deposition of final surface promoter layer and c) coating G - 10% functionalised carbon nanotube content with use of an interlayer; no deposition of final surface promoter layer; prior to any ice growth or detachment.

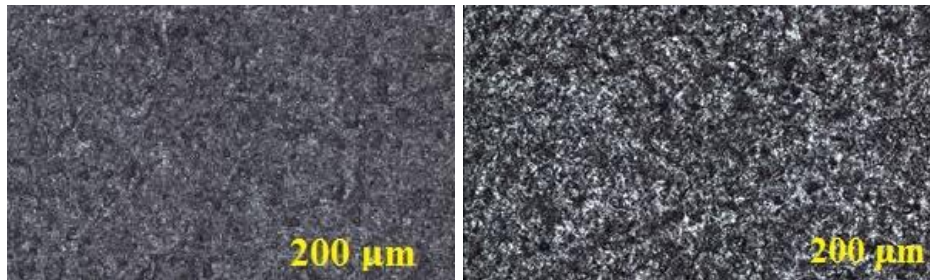


Figure 3. a) Coating E - 20% functionalised carbon nanotube content with use of an interlayer; no deposition of final surface promoter layer and b) coating G - 10% functionalised carbon nanotube content with use of an interlayer; no deposition of final surface promoter layer under Alicona optical microscope at 20x magnification.

Figure 4 shows the centrifuge system employed to evaluate the adhesion strength of a controlled ice sample to each coated substrate. In essence, a rotor holding the ice/substrate sample was spun at increasing rotation rates. When the centripetal acceleration on the ice sample, induced by the rotor's rotation, overcomes the adhesion strength of the ice to the substrate, the ice detaches from the substrate. Thus, the adhesion strength of ice to the substrate can be estimated as $F = m r \omega^2$ where m is the mass of ice, r is the rotor length and ω is the speed of rotation at detachment in $\text{rad}\cdot\text{s}^{-1}$. As a shear stress, the adhesion stress is $\tau = F/A$, where A is the ice/substrate contact area.

This permits relative measurements of coated sample adhesion shear stress τ_c , compared with a reference sample τ_u , quantifying the performance of coatings in reducing ice adhesion. This term

is defined as the adhesion reduction factor $ARF = \tau_u/\tau_c$ ⁹. A coating leading to lower rotation speed at detachment for a specified ice type, will thus be more icephobic than a corresponding coating with detachment at a higher rotation speed.

The centrifuge apparatus (Figure 4) comprises a stainless steel cylindrical drum, 300 mm deep, diameter 500 mm. A motor is mounted beneath a steel floor within the drum, 150 mm below its top rim, with the shaft passing through the floor. This system was placed in an environment-controlled chamber (Design Environmental ALPHA 1550-40H) where the ambient temperature of the test could be controlled.

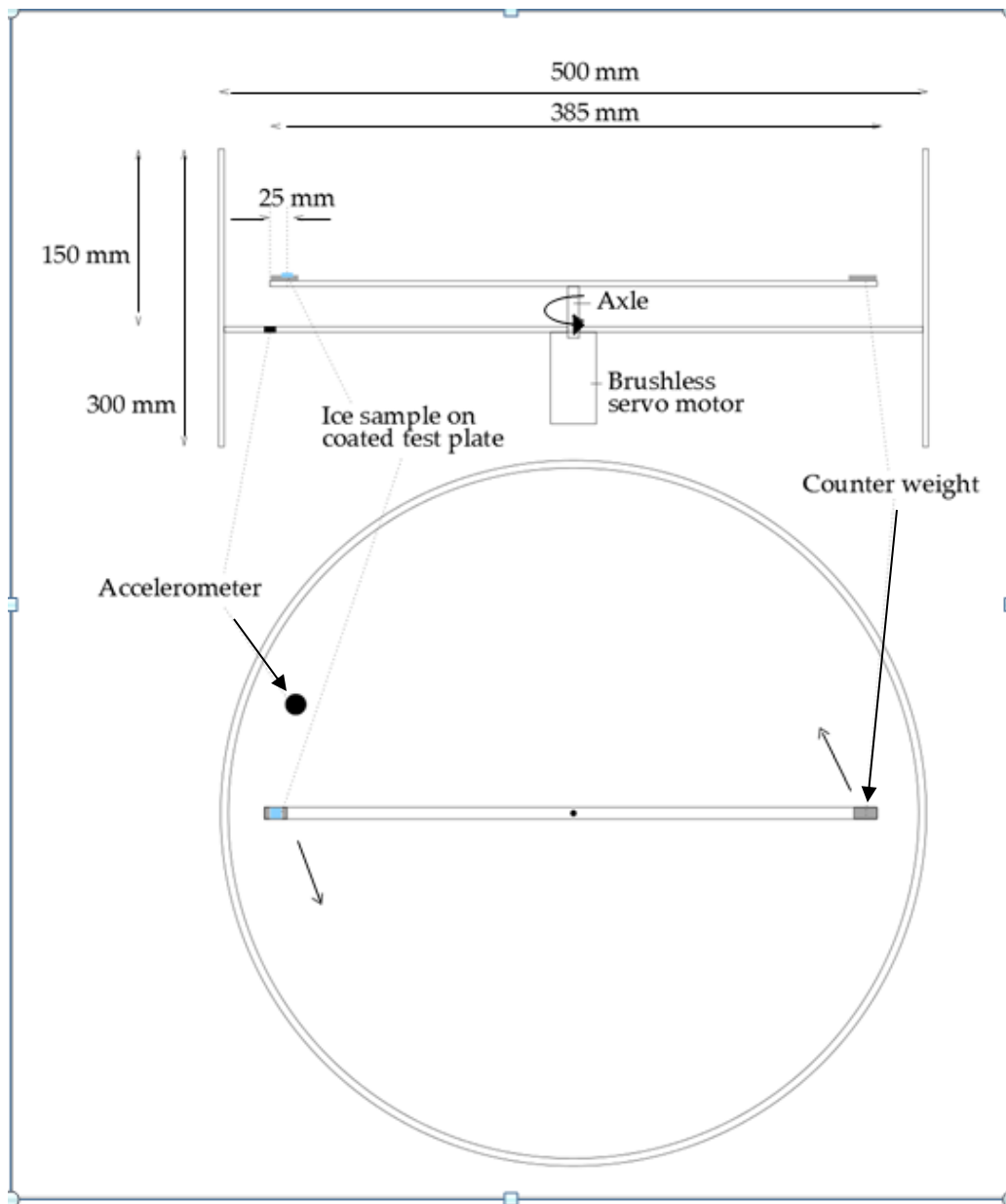


Figure 4. Schematic diagram of the centrifuge ice adhesion test device. This consists of a carbon fibre rotor driven by a brushless servo motor and housed in a stainless steel casing. The ice/substrate sample is affixed to one end of the rotor and spun at increasing rates until detachment.

A carbon fibre reinforced polymer rotor (selected to minimize rotor inertia) with an ice/substrate sample affixed as described in the next paragraph and with dimensions 385 x 20 x 3 mm was mounted on the motor shaft via a stiff coupling. The rotor was driven by a servo motor (MOOG

G403-2053A) at steady accelerations of 30 rpm/s from zero up to the motor's maximum speed of 4500 rpm. This motor was selected for performance at the sub-zero temperatures at which the ice adhesion tests were carried out, designed to withstand condensation formation within the motor housing, and using a resolver control. An accelerometer was mounted in the drum floor to detect ice detachment and a microphone was placed underneath the drum to corroborate the time from initiation, and thus rotation rate, at ice detachment.

To generate repeatable uniform glaze ice samples the sample substrate plate was attached to the rotor with a counterweight fixed to the other end to prevent undesirable vibrations when spinning the rotor. The arm was placed upside down such that the central, coated 20 x 30mm portion of the substrate plate was in contact with de-ionised 18 M Ω Ultrapure UV filtered water held in a 2 ml silicone mould. This was left in the environment-controlled chamber at -5°C for 24 hours, to produce repeatable samples of pure glaze ice on each sample substrate.

Glaze icing occurs when supercooled droplets do not freeze on impact with an aircraft wing; but run back before freezing to form a smooth, clear structure²⁷. Glaze ice was chosen in our experiment because in reality, it is much harder to remove from a surface than rime, providing an upper bound measurement for ice adhesion. Further, glaze generally forms on regions of the wing for which these coatings are designed and also because consistent glaze samples can be grown artificially, we can measure adhesion more repeatedly than would be achievable with rime ice samples.

The adhesion strength of a glaze ice sample, grown as described above, on 20 uncoated Al 6082-T651 substrates was measured under nominally identical ice preparation and adhesion test

conditions (-5°C) to evaluate the repeatability of the preparation and test method. The characteristics of the 20 samples and their adhesion strength over 33 tests, are shown in Table 2.

Table 2. Properties and their variation across 20 uncoated substrates illustrating the repeatability of each measurement.

Property	Mean and standard deviation for 20 samples
Static Contact Angle	93.2 ± 2.63° (SD = 2.82%)
Advancing Contact Angle	100 ± 5.33° (SD = 5.33%)
Receding Contact Angle	35.7 ± 4.90° (SD = 13.7%)
Contact Angle Hysteresis	64.5 ± 5.54° (SD = 8.59%)
Roughness	0.266 ± 0.051 μm (SD = 19.0%)
Detachment speed	4210 ± 270 rpm (SD = 6.48%)
Adhesion strength	152 ± 20.0 kPa (SD = 13.2%)

Note that the repeatability of this adhesion strength test compares favourably with previous, similar measurements⁸. We believe that this is partly due to the method employed for growing ice on the substrates that yields a repeatable layer of glaze ice at contact with only rare imperfections such as cracks or air inclusions.

A crucial element of the current work is to consider the durability of the coatings, thus the process surface characterization (Table 1), ice growth, ice detachment through the adhesion test was repeated 10 times (17 for the non-conductive coatings) for each coated substrate.

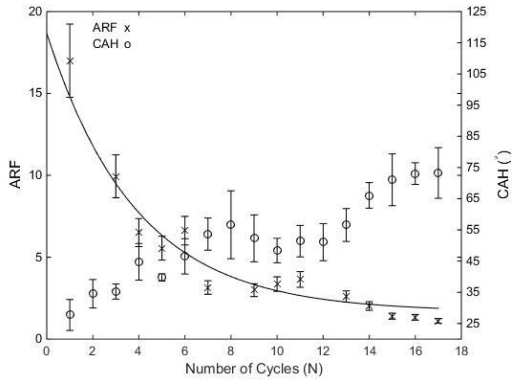
4. Results and Analysis

The performance of coatings A—K, as indicated by their adhesion reduction factor (ARF) and contact angle hysteresis (CAH), was evaluated over 10 cycles (17 cycles for A—D) of ice growth and detachment, shown in Figure 5. These data show qualitatively that adhesion reduction factor is correlated with CAH. As the sample goes through successive cycles of ice growth and detachment its icephobicity, as indicated by adhesion reduction factor, reduces and the CAH increases – this observation is discussed in more detail in the analysis section. Data where the adhesion test failed due to e.g. only partial detachment of the ice from the rotor, or poor attachment of the mould to the substrate when growing the ice, are not included (for example coating A, cycle 8, Figure 5).

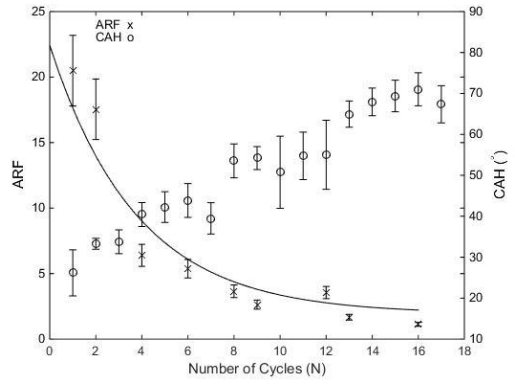
To evaluate the reduction in performance of the coatings with use, the adhesion reduction factor after cycle N , $ARF(N)$, was fitted as an exponential decay

$$ARF(N) = ARF(1)(e^{-N\alpha} + C), \quad (1)$$

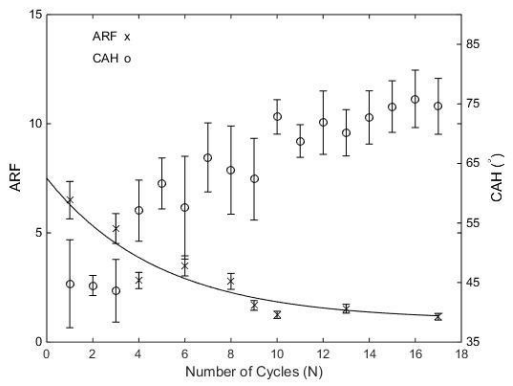
where α is a *coating durability rate* and C characterizes the *retained icephobic fraction* of the sample after many cycles i.e. $ARF(1).C$ is the projected adhesion reduction factor of the coating as the number of cycles, N , tends to infinity. This retained icephobicity thus characterizes the long term chemical and/or surface finish alteration to the substrate surface the coating has made.



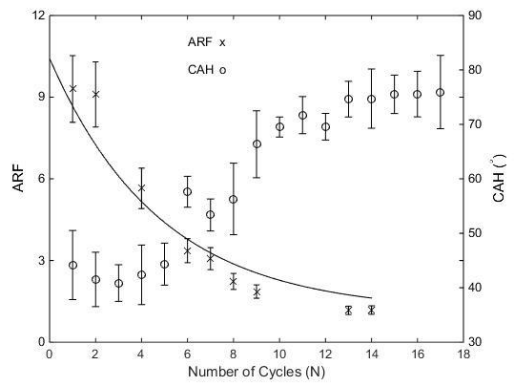
a)



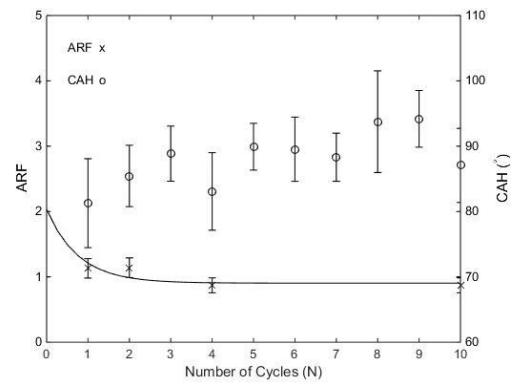
b)



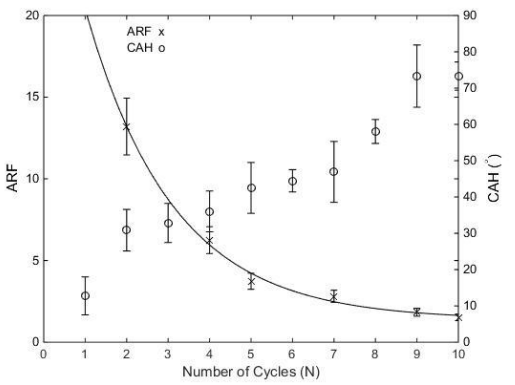
c)



d)



e)



f)

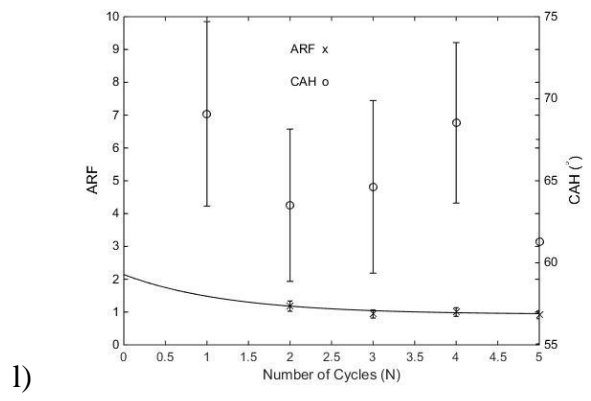
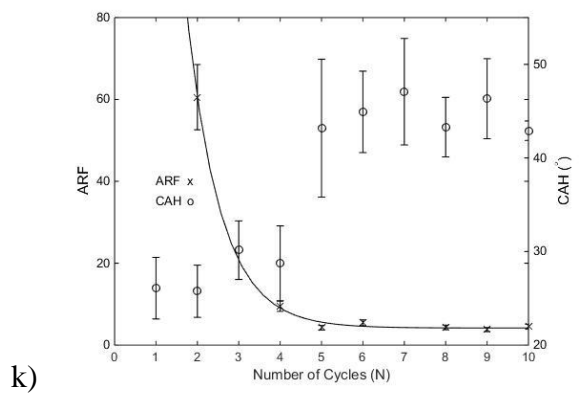
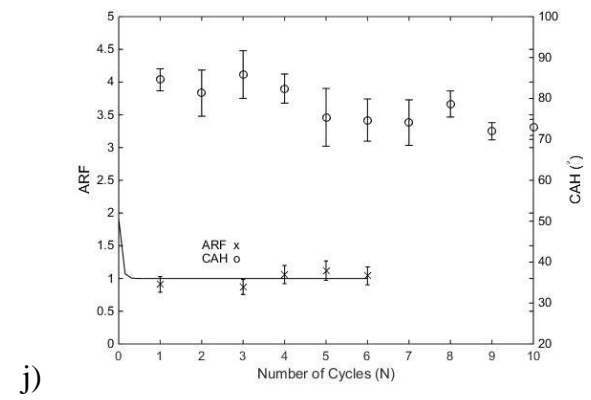
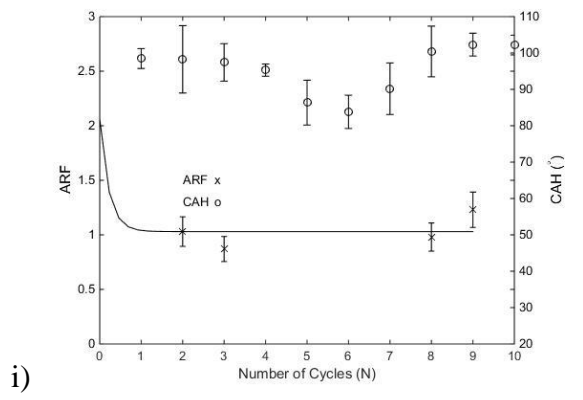
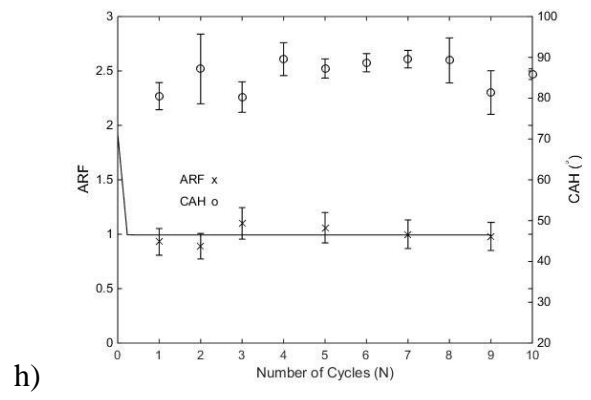
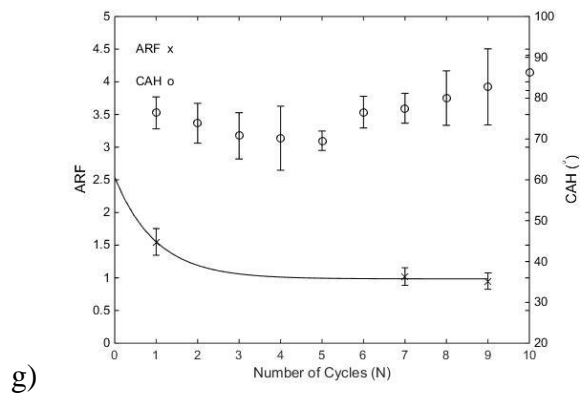


Figure 5. a) Coating A (Initial Adhesion Strength = 8.9 ± 1.2 kPa), b) Coating B (Initial Adhesion Strength = 7.4 ± 1 kPa), c) Coating C (Initial Adhesion Strength = 23.4 ± 3.1 kPa), d) Coating D (Initial Adhesion Strength = 16.3 ± 2.2 kPa), e) Coating E (Initial Adhesion Strength = 138.2 ± 18.2 kPa), f) Coating F (Initial Adhesion Strength = 7.5 ± 1 kPa*), g) Coating G (Initial Adhesion Strength = 98.1 ± 12.9 kPa), h) Coating H (Initial Adhesion Strength = 163.4 ± 21.5 kPa), i) Coating I (Initial Adhesion Strength = 147.6 ± 19.4 kPa*), j) Coating J (Initial Adhesion Strength = 167 ± 22 kPa), k) Coating K (Initial Adhesion Strength = 0.8 ± 0.1 kPa*) and l) uncoated substrate (Initial Adhesion Strength = 126.7 ± 16.7 kPa*). Variation in adhesion reduction factor and contact angle hysteresis with cycles of ice growth and detachment. Adhesion reduction factor has been fitted to find durability rate and retained icephobicity (equation (1)). * refers to extrapolated values since test results from first cycle were invalid.

From Figure 5, Coating K qualitatively appears to have performed the best over the initial portion of the test period. The 3 highest adhesion reduction factors were measured for Coating K (60.55) and Coating B (20.5, 17.5) in the first and first two cycles respectively, corresponding to highest levels of icephobicity. From Table 3 however, we can see that the retained icephobicity of A and B is significantly greater than K. Since the results for A, B, C and D are within the error limits for ARF itself (i.e. 13.2%), the repeatability and accuracy of our test procedure is confirmed since the two types of coatings were produced under identical conditions.

Figure 5l) shows the performance of an uncoated substrate over 5 cycles. We can see that there is practically no change in the surface characteristics and ARF value of the substrate due to the repeated adhesion and removal of ice. This also confirms the fact that several coatings (E, G, H, I and J) behave like an uncoated substrate with poor icephobicity.

Table 3. Coating decay rates and retained icephobicity values of Coatings A—K and uncoated substrate L.

Coating	Coating durability rate, α	Initial ARF, ARF_I	Retained icephobicity, $C.ARF_I$	Ranking (min α)	Ranking (max C)
A	0.26	17.00	1.7	3	2
B	0.27	20.50	1.8	4	1
C	0.21	6.50	1.0	1	5
D	0.22	9.30	1.1	2	4
E	1.30	1.10	0.9	9	10
F	0.47	20.40*	0.9	5	10
G	1.00	1.55	1.0	7	5
H	27.20	0.93	1.0	12	5
I	4.65	1.03*	1.0	10	5
J	14.10	0.91	1.0	11	5
K	1.22	197.1*	1.3	8	3
L	0.78	1.2*	0.8	6	12

*Extrapolated values since test results from first cycle were invalid.

Table 3 shows initial adhesion reduction factor ($ARF(I)$) together with the coating durability rates, α , and retained icephobicity, ($ARF(N)$), derived from a least squares optimization to the fit equation (1).

Of the silica nanoparticle coatings, the additional heat treatment of 2 hours at 550°C during preparation of coatings C and D, compared with coatings A and B appears to have reduced the icephobic properties. The initial adhesion reduction factor ($ARF(I)$) of coating C is 2.6 times less than for coating A and 3.1 times less than coating B respectively. Similarly, for coating D, the initial adhesion reduction factor is 1.8 times less than coating A and 2.2 times less than coating B.

However, the heat treated coatings C and D have a slower wear rate than coatings A and B. This implies that the additional heat treatment reduced the initial icephobic quality of the surface but ensured that surface has a longer durability than A and B.

Carbon nanotube coatings E, G, H, I and J had low levels of icephobicity since, in multiple adhesion tests, the ice did not detach from the rotor by the time the maximum speed was reached (4500 rpm). Although all five coatings were hydrophobic, the CAH was initially high (listed in Table 1) and remained high over the test cycles. During the 4 adhesion tests for coating E where the ice did detach, the adhesion reduction factor was in the range 0.87-1.15, evidencing the low icephobicity. However, for this coating the CAH varied very little, remaining at $88.08 \pm 4.14^\circ$ over the 10 cycles. This shows that the coating has maintained its surface properties well over the cycles. Similarly, for coating G in 3 successful tests, the adhesion reduction factor remains in the range 0.95-1.55, exhibiting low icephobicity, and the coating also maintained its surface properties well over the test cycles. H, I and J showed similar characteristics during the test period.

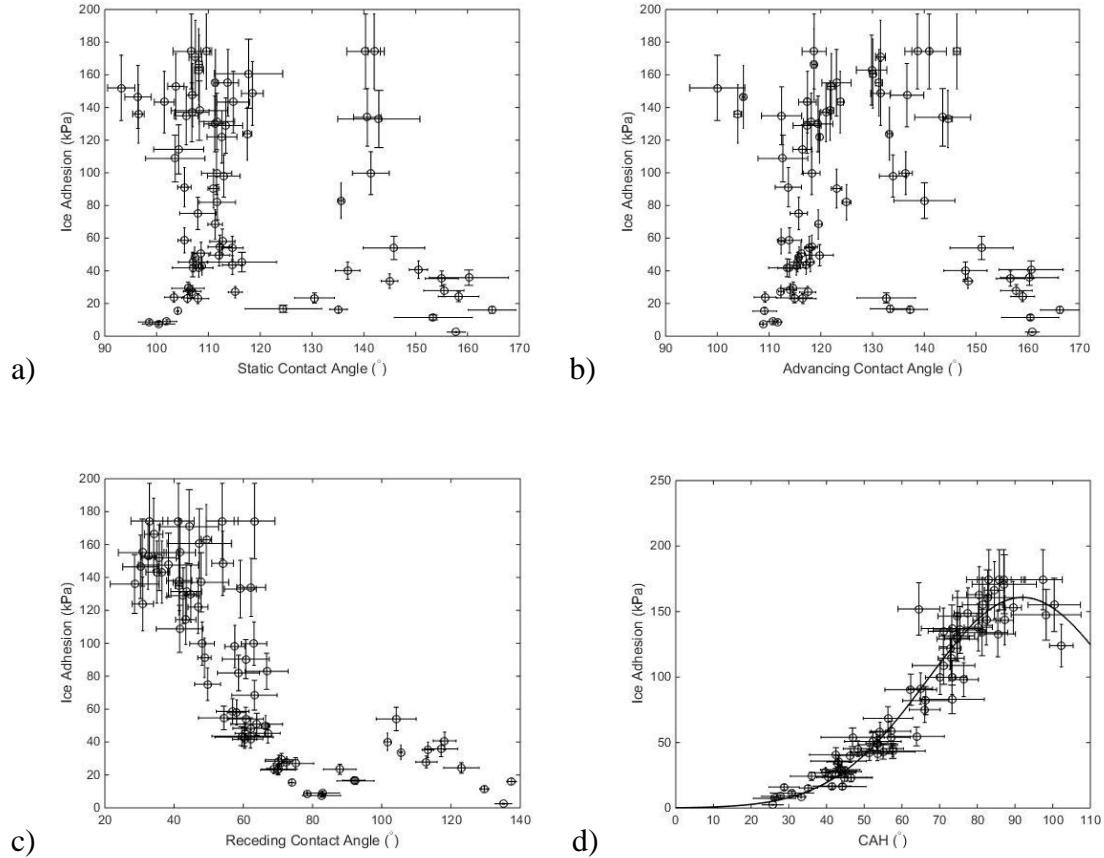


Figure 6. Ice adhesion versus a) Static contact angle, b) Advancing contact angle, c) Receding contact angle, d) Contact angle hysteresis, for all 11 coatings and the uncoated substrate.

Figure 6 shows the ice adhesion versus static, advancing, receding and contact angle hysteresis for all 11 coatings and 20 uncoated substrates throughout the test period for ready comparison to the literature (8, 9, 26—28). The best fit was found to be a Gaussian curve with relation to the change in ice adhesion versus CAH (figure 6d). The equation of the Gaussian fit is given as:

$$Y = A e^{\frac{-(X-B)^2}{c^2}} \quad (2)$$

Where the coefficients (with 95% confidence bounds) are: $A = 160.8$ kPa (152.4 kPa, 169.2 kPa), $B = 91.97^\circ$ (88.42°, 95.53°) and $C = 35.76^\circ$ (32.18°, 39.34°). Importantly, we see that the ice adhesion strength increases with respect to CAH to a maximum value of 160.8 kPa at 91.97° ($\sim 92^\circ$). The reason for this can be explained by the increased ice-coating contact area that would be apparent for coatings having a high CAH. In figure 6d), when $CAH > \sim 92^\circ$, the adhesion strength reduces with increase in CAH. The reason for this phenomenon in the trendline is that coatings with high CAH coupled with high surface roughness, can cause pockets of air bubbles to form at the ice/coating interface²⁸; thereby reducing adhesion strength. Importantly, figure 6d) indicates that already at CAH values of $\sim 25^\circ$, adhesion strength is close to zero.

Kulinich and Farzaneh²⁹ exhibit a linear fit for adhesion strength versus CAH but the fit covers a smaller CAH range and only 10 data points. Meuler et al. (2010)³⁰ find a linear correlation between adhesion strength and a parameterized CAH x-axis i.e. $\cos(\theta_{\text{rec}} - \theta_{\text{adv}})$; but consider only cases with $\theta_{\text{adv}} > 105^\circ$ and the fit does not extend to the origin. When $\theta_{\text{adv}} < 100^\circ$, the ice adhered much more strongly to the substrate than anticipated according to the fit. They also find a linear fit with adhesion strength versus $(1 + \cos\theta_{\text{rec}})$ plotting data from 22 substrates when the adhesion strength and contact angle parameters were calculated only once for each substrate result. Our results however indicate that two surfaces with similar receding angles (55° and 105°) can have similar adhesion strengths (see Figure 6c); and it is the CAH which is the dominant parameter determining adhesion strength. It must be noted that figure 6d) exhibits the degradation of the coating and the plot of the subsequent change in adhesion strength with measurements of contact angle parameters for the coatings. This is in contrast to Meuler et al. (2010)³⁰ who calculate adhesion strength and contact angle parameters only once for each substrate result. No apparent trend can be seen with respect to static and advancing contact angle with regards to the ice adhesion

implying the interaction of water with a surface is very different to the interaction of that same surface with ice. This has been well corroborated in the literature^{9, 29, 30}. Results from our test period corroborate this, since certain hydrophobic coatings behaved “icephillic” when exhibiting high CAH.

From Figure 6 and observations during testing, it is also apparent that repeated tests using the centrifuge with the ice shearing off the coating surface, had a minimal impact on changes in the static and advancing contact angles as compared to the more pronounced changes (reduction) in the receding contact angle in coatings A, B, C, D, F and K. For coatings E, G, H, I and J; static, advancing and receding values stayed near constant through the test period with poor icephobicity. This finding leads to an overall dominant impact of the CAH on the ice adhesion strength but it is an interesting phenomenon to explore. The reason for the change in receding angle with repeated tests as compared to static and advancing contact angle could be the method of removal of the ice sample as it shears off and removes part of the coating surface (as noticed on visual observation). The receding contact angle would be affected more than the static and advancing contact angle due to its more intricate dependence on time since it is a measurement of “de-wetting”. It is possible that the shearing of the ice exposed the encapsulated air pockets in the coatings due to deposition of the nanoparticles. The increased surface area would affect the receding angle greatly and the time taken for the de-wetting process.

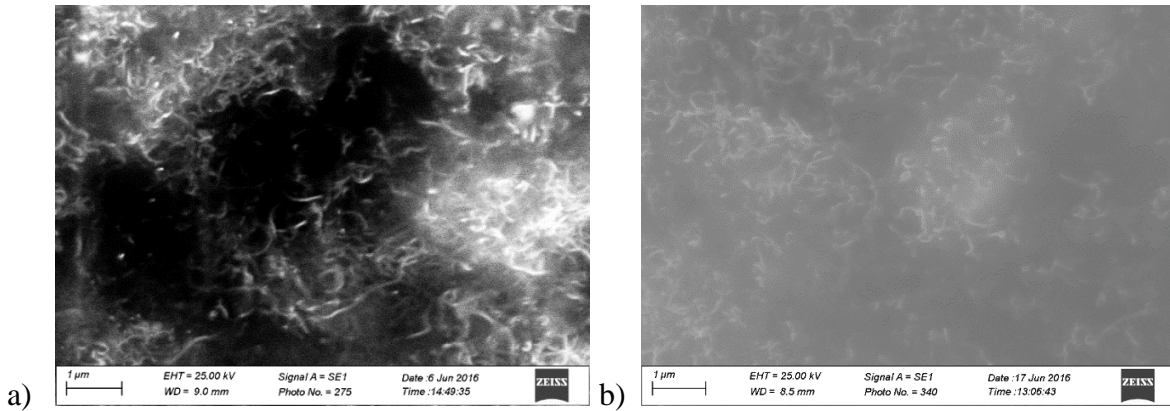


Figure 7. SEM micrographs of sample H at a magnification of 30000X obtained before (a) and after (b) the ice adhesion tests.

Figure 7 shows the SEM micrographs of coating H before (a) and after (b) the ice adhesion tests. CNTs are clearly visible in both micrographs while a smoother surface remains after the ice adhesion tests. The procedure of surface smoothing may be attributed to removal of bigger CNT bundles protruding from the outer part of the coating as shown in Fig 7a which have been removed with ice following a mechanism proposed by Ling et al. (2016)³¹. They observed that during freezing, the tips of the carbon nanotubes deposited on stainless steel substrate become embedded within the ice phase and are ripped off of the substrate when the ice column is sheared from the mesh. However, in our case, such a mechanism, if present, is limited as we can still observe the presence of CNTs after the ice adhesion testing. This is because in our case the CNTs coating is well adhered to the aluminum substrate and retains its integrity after multiple cycles of icing-deicing.

5. Conclusions

The anti-icing performance of 11 coatings, some with silica nanoparticles and others incorporating carbon nanotubes, has been evaluated; candidates for application to the surface of aircraft wings to prevent the accretion of runback ice. The ice adhesion strength, together with the

development of surface characteristics, was measured over multiple cycles of glaze ice growth and detachment from the coated substrate. The development of icephobicity was characterized by a *retained icephobicity*, that is the long term chemical or mechanical alteration the coating has made to the substrate surface, and a *durability rate*. These data showed that initially strong icephobic performance typically wears quickly, and that the retained icephobicity is not necessarily linked to initial coating performance. Thus, for the silica nanoparticle and polystyrene coatings, heat treatment led to reduced initial and long term icephobicity in comparison with the non-heat treated equivalents, however, the durability rate of the former was lower than the latter. For the carbon nanotube composite coatings, best results were obtained for the coating with 5% functionalised carbon nanotube content with use of an interlayer between the coating and the substrate and deposition of a final surface promoter. In support of findings from previous studies⁹, increasing ice adhesion is well correlated to increasing contact angle hysteresis up to CAH = $\sim 92^\circ$. Lower CAH reduces the ice-solid area of contact and thus the energy of the adhesive bond. Above CAH of $\sim 92^\circ$, our data indicates from figure 6d) that adhesion strength reduces. This could be due to the presence of air pockets on rough surfaces contributes to reducing the bond between ice and the surface and requires further investigation. Importantly, at CAH values of $\sim 25^\circ$, the adhesion strength is very close to zero; indicating a reduced effect of lower CAH values than previously assumed. Icephobicity does not necessarily correlate with hydrophobicity. The greater reduction in receding contact angle as compared to static and advancing contact angle over the test period can be attributed to the fact that the removal of ice affects the surface characteristics of the coatings, increasing the surface area of contact and eventually increasing time for the de-wetting process. For runback icing in particular, high static and advancing contact angles are recommended to

prevent wetting by runback water before it eventually freezes. To reduce the ice adhesion after freezing, the surface should possess high receding contact angle and low CAH.

AUTHOR INFORMATION

Author Contributions

The manuscript was written through contributions of all authors. All authors have given approval to the final version of the manuscript.

Acknowledgement

This work was supported by CleanSky-EU initiative ICECOAT. The work forms a part of the project to develop a suitable smart icephobic, hydrophobic and insect-repellent coating to coat aircraft wing surfaces.

REFERENCES

- (1) Thomas, S.K.; Cassoni, R.P.; MacArthur, C.D. Aircraft anti-icing and de-icing techniques and modelling. *Journal of Aircraft* **1996**, 33:5, 841—854.
- (2) Kasaai, M.R.; Farzaneh, M. A critical review of evaluation methods of ice adhesion strength on the surface of materials. Proceedings of OMAE04, 23rd International Conference on Offshore Mechanics and Arctic Engineering, June 20—25, Vancouver, British Columbia, Canada, **2004**, ASME.
- (3) Anderson, D.N.; Reich, A.D. Tests of the performance of coatings for low ice adhesion. 35th Aerospace Sciences Meeting and Exhibit AIAA, Reno, Nevada, **1997**.
- (4) Susoff, M.; Siegmann, K.; Pfaffenroth, C.; Hirayama, M. Evaluation of icephobic coatings—Screening of different coatings and influence of roughness. *Applied Surface Science*, **2013**, 282, 870—879.

- (5) Gohardani, O.; Hammond, D.W. Ice adhesion to pristine and eroded polymer matrix composites reinforced with carbon nanotubes for potential usage on future aircraft. *Cold Regions Science and Technology*, **2013**, 96, 8—16.
- (6) Kraj, A.G.; Bibeau, E.L.; Measurement method and results of ice adhesion force on the curved surface of a wind turbine blade. *Renewable Energy*, **2010**, 35, 741—746.
- (7) Strobl, T.; Raps, D.; Hornung, M. Comparative evaluation of ice adhesion behaviour. *World Academy of Science, Engineering and Technology*, **2012**, 68, 1673—1678.
- (8) Laforte, C.; Beisswenger, A. Icephobic material centrifuge adhesion test. 11th International Workshop on Atmospheric Icing on Structures, Montreal, Canada, **2005**.
- (9) Kulinich, S.A.; Farzaneh, M. Ice adhesion on super-hydrophobic surfaces. *Applied Surface Science*, **2009**, 255, 8153—8157.
- (10) Jin, Z.; Hu, H. Icing process of small water droplets impinging onto a frozen cold plate. *Journal of Thermophysics and Heat Transfer* **2010**, 24:4, 841—844.
- (11) Sayward, J.M.: Seeking low ice adhesion. Special Report 79-11, Cold Regions Research and Engineering Laboratory, Corps of Engineers, United States Army, Hanover: New Hampshire **1979**.
- (12) Li, H.; Li, X., Luo, C.; Zhao, Y.; Yuan, X. Icephobicity of polydimethylsiloxane-b-poly (fluorinated acrylate). *Thin Solid Films* **2014**, 573, 67—73.
- (13) Jafari, R.; Menini, R.; Farzaneh, M. Superhydrophobic and icephobic surfaces prepared by RF-sputtered polytetrafluoroethylene coatings. *Applied Surface Science*, **2010**, 257, 1540-1543.

- (14) Zhang, K.; Li, X.; Zhu, K.; Li, Y.; Tao, C, Yuan, X. UV-curable POSS-fluorinated methacrylate diblock copolymers for icephobic coatings. *Progress in Organic Coatings* **2016**, 93, 87—96.
- (15) Li, X.; Zhao, Y.; Li, H.; Yuan X. Preparation and icephobic properties of polymethyltrifluoropropylsiloxane-polyacrylate block copolymers. *Applied Surface Science*, **2014**, 316, 222—231.
- (16) Li, Y.; Luo C.; Li, X.; Zhang, K.; Zhao, Y.; Zhu, K.; Yuan, X. Submicron/nano-structured icephobic surfaces made from fluorinated polymethylsiloxane and octavinyl-POSS. *Applied Surface Science*, **2016**, 360, 113—120.
- (17) Menini, R.; Farzaneh, M. Elaboration of Al₂O₃/PTFE icephobic coatings for protecting aluminum surfaces. *Surfaces & Coatings Technology*, **2009**, 203, 1941—1946.
- (18) Wang N., Xiong D., Deng Y., Shi Y., Wang K. Mechanically robust superhydrophobic steel surface with anti-icing, UV-durability and corrosion resistance properties. *ACS Applied Materials & Interfaces*, **2015**, 7, 6260—6272.
- (19) Wang N., Xiong D., Lu Y., Pan S., Wang K., Deng Y., Shi Y. Design and fabrication of the lyophobic slippery surface and its application in anti-icing. *The Journal of Physical Chemistry C*, **2016**, 120, 11054—11059.
- (20) Jung, S. et al. Are superhydrophobic surfaces best for icephobicity? *Langmuir*, **2011**, 27, 3059—3066.
- (21) Nosonovsky, M.; Hejazi, V.; Why superhydrophobic surfaces are not always icephobic. *ACS Nano*, **2012**, 6, 8488—8491.
- (22) Kulinich, S.A.; Farhadi, S.; Nose, K.; Du, X.W. Superhydrophobic surfaces: Are they really ice-repellant? *Langmuir*, **2011**, 27, 14143—14150.

- (23) Zhang, L.; Wu, J.; Hedhili, M.N.; Yang, X.; Wang, P. Inkjet printing for direct micropatterning of a superhydrophobic surface: toward biomimetic fog harvesting surfaces. *Journal of Materials Chemistry A*, **2015**, 3, 2844—2852.
- (24) Cao, L., Jones, Andrew K., Sikka, Vinod K., Wu, Jiangzhong, Gao, Di, Anti-icing superhydrophobic coatings. *Langmuir*, **2009**, 25:21, 12444-12448.
- (25) Della Volpe, C.; Siboni, S.; Morra, M. Comments on some recent papers on interfacial tension and contact angles. *Langmuir*, **2002**, 18:4, 1441-1444.
- (26) Drelich, J. Guidelines to measurements of reproducible contact angles using a sessile-drop technique. *ice | science*, **2013**, 1—7. DOI: 10.1680/si.13.00010.
- (27) Politovich, M.K. Aircraft Icing. *Encyclopedia of Atmospheric Sciences*, **2003**, 68-75.
- (28) Guerin F., Laforte C., Farinas M-I., Perron J. Analytical model based on experimental data of centrifuge ice adhesion tests with different substrates. *Cold Regions Science and Technology*, **2016**, 121, 93—99.
- (29) Kulinich S.A., Farzaneh M. How wetting hysteresis influences ice adhesion strength on superhydrophobic surfaces. *Langmuir*, **2009**, 25(16), 8854—8856.
- (30) Meuler A.J., David Smith J., Varanasi K.K., Mabry J.M., McKinley G.H., Cohen R.E. Relationships between water wettability and ice adhesion. *ACS Appl. Mater. Interfaces*, **2010**, 2(11), 3100—3110.
- (31) Ling E.J.Y., Uong V., Renault-Crispo J-S., Kietzig A-M., Servio, P. Reducing ice adhesion on nonsmooth metallic surfaces: wettability and topography effects, *ACS Applied Materials & Interfaces* 8, **2016**, 8789—8800.